

We are IntechOpen, the world's leading publisher of Open Access books Built by scientists, for scientists

6,900

Open access books available

185,000

International authors and editors

200M

Downloads

Our authors are among the

154

Countries delivered to

TOP 1%

most cited scientists

12.2%

Contributors from top 500 universities



WEB OF SCIENCE™

Selection of our books indexed in the Book Citation Index
in Web of Science™ Core Collection (BKCI)

Interested in publishing with us?
Contact book.department@intechopen.com

Numbers displayed above are based on latest data collected.
For more information visit www.intechopen.com



Surface Plasmons on Complex Symmetry Nanostructured Arrays

Brian Ashall and Dominic Zerulla

Additional information is available at the end of the chapter

<http://dx.doi.org/10.5772/51336>

1. Introduction

In recent years it has become accepted that the direction of the plasmonics community is becoming increasingly applied. This is a natural progression, whereby scientific advances are inevitably applied to appropriate technologies. Indeed, in order for the community of plasmonics to continue growing, or at least to maintain the current status, real world technological applications are required. However, this is not to say that the level of fundamental SP research will decrease, as there are still many questions to be answered or clarified on a fundamental level. The dramatic growth of plasmonics in the modern era can be predominantly contributed to four components: nanoscale fabrication techniques, computation power, SPP applications, and "the promise of plasmonics" [1].

The focus of this chapter draws inspiration from all four of the above points. In particular, following an introduction and description of nanostructure fabrication techniques and design considerations in the first section, the second section will detail farfield analysis techniques used for the examination of the light diffracted from structured arrays, and the subsequent identification of plasmons based on their farfield signatures. Following this, the excitation of SPPs on tailor designed 3 fold symmetric structures will be discussed, with advantages resulting from this symmetry breaking explored. Unlike rotationally symmetric structures, such 3-fold symmetric structures are inherently capable of symmetry breaking as a result of their orientational dependencies. In particular, this section (Sec. 3) will focus on the engineering of the SPP nearfield distributions on complex nanostructures. For this, the use of a PEEM (Photo Emission Electron Microscope) to map the plasmon nearfields on the surface of an array of the structures will be presented. It will be shown that the location and intensity of the focused nearfields can be controlled by changing the polarisation of the excitation light, enabling the switching of the plasmon energy localisation [2]. In section 4, specific symmetry and geometric properties of nanostructures will be shown to have an impact on the propagation of SPPs. In particular, it will be demonstrated and justified how in certain orientations, arrays of rotor shaped nanostructures have interesting wave-guiding interactions with propagating SPPs [3]. One result of this is a shift from P polarised

illumination at which the classical farfield SPP related minimum reflectivity occurs. Following this, the first instance of plasmon mediated polarisation reorientation observed in the farfield, with no associated directional change of the farfield light, will be described and accompanied by supporting simulations [4, 5]. Finally, section 5 will deal with aspects of ultrafast dynamics of propagating SPPs. In particular, a tailor designed architecture will be examined for the possibility of generating broadband, ultrashort plasmon pulses [6]. Furthermore, the temporal modification of the illumination pulse resulting from SPP excitation will be investigated.

2. Plasmon active nanostructures and their fabrication

The field of plasmonics has taken a big leap in recent years, with one of the major attributors being the development of techniques to fabricate the micro- and nano-structures needed to control the flow and storage of electromagnetic energy on a very small scale. This local excitation and control of SPPs requires structuring techniques with nanoscale precision, of which electron-beam lithography and focused ion beam irradiation have proven to be the most important because of their ability to make diverse structures with high resolution. In this section, these structuring techniques will be briefly discussed, along with the implications of sample quality.

2.1. Nanostructuring

Electron-Beam Lithography (EBL) is a process that uses a focused beam of electrons to form patterns for material deposition on (or removal from) the sample substrate. In comparison to optical lithography, which uses light for the same purpose, EBL offers higher patterning resolution because of the shorter wavelength possessed by the 10-50 keV electrons that it employs. This small diameter focused beam of electrons is scanned over a surface, negating the need for masks required in optical lithography for the projection of patterns. An EBL system simply draws the pattern over the resist wafer using the electron beam as its drawing pen. Thus, EBL systems produce the resist pattern in a serial manner. This makes it slow compared to optical systems, but gives a user more control of the structure shape and allows for different rate of lithography at different locations.

The *Focused Ion Beam* (FIB) technique was developed during the late 1970s and the early 1980s, with the first commercial devices available in the late 1980's [7]. The technology enables localised milling and deposition of conductors and insulators with high precision, hence its success in device modification, mask repair, process control and nanopatterning [8–10]. When energetic ions hit the surface of a solid sample, they lose energy to the electrons of the solid as well as to its atoms. The most important physical effects of incident ions on the substrate are: sputtering of neutral and ionized substrate atoms (this effect enables substrate milling), electron emission (this effect enables imaging), displacement of atoms in the solid (induced damage) and emission of phonons (heating). Chemical interactions include the breaking of chemical bonds, thereby dissociating molecules (this effect is exploited during deposition). The best resolution of FIB imaging and milling is comparable to the minimum ion beam spot size, typically below 10 nm. In crystalline materials, such as aluminium and silver, the ion penetration depth varies due to channeling along open columns in the lattice structure. The removal of sample material is achieved using a high ion current beam, resulting in a physical sputtering of sample material. By scanning the beam over the substrate, an arbitrary shape can be etched.

Thin Metal Films: A basic requirement for experimental research on SPPs is the ability to make high purity, smooth, and often thin, metallic films. A number of techniques are available for this, the most typical being resistive thermal evaporation and e-beam evaporation.

The principle of vacuum evaporation is simple: the substrate and the coating material are both placed in an evacuated enclosure, some distance apart. The coating material is then heated to its vaporisation pressure point, so that it evaporates. Sufficient thermal energy is supplied to enable individual atoms to escape from the surface of the molten material. These atoms travel in a straight line through the vacuum towards the substrate where they adhere to the surface. Several methods may be used to melt the evaporant, such as resistive heating in which the evaporant is loaded in a boat shaped crucible made of a metal with a considerably higher melting point than the evaporant, through which a large DC current is passed. Many metals may be evaporated very successfully using resistive heating, and of particular importance here, this list includes Silver, Gold, Aluminium, Nickel, Platinum and Chromium; some of which are important as plasmon active substrates, and others important for adhesion layers [11].

An alternative deposition technique is electron beam heating. Here, a hot wire filament is used as a thermionic electron emitter, where the electrons are accelerated and guided toward the evaporant (either directly, or contained in a crucible). The evaporant is heated by the kinetic energy of the electrons and subsequently is coated on the sample. This method can typically generate smoother films in comparison to the resistive heating method, as the material is evaporated from its surface in a much more controlled manner than resistive heating, where the sample is typically completely melted and prone to sputtering.

In either system, the rapid condensation typically produces grained films which are relatively rough on an atomic scale, but on the scale of the wavelength of the radiation they are typically very smooth. Therefore, roughness induced re-radiation of an excited plasmon will be at an acceptably low level for the majority of plasmon experiments.

2.2. Three fold symmetric structures

Experimental examinations presented in this chapter primarily deal with arrays of structures of 120° symmetry properties, along with a reference sample of a more typical geometry (ring or doughnut shape). The geometry of four example structures are depicted in Fig. 1. They are designed such that they relinquish the widely investigated circular symmetry in favor of a 120° , or 3 fold, symmetry. One of the primary and original concepts behind this 3 fold symmetry design is that it permits the reduction of the footprint of the structure in comparison to a ring design, while maintaining surface plasmon resonance conditions. For a ring shape structure, an optimum nearfield resonance will occur where the ring diameter is an (low) integer multiple of the plasmon wavelength. If this is the case, a plasmon propagating around the structure will not destructively interfere with itself, but instead each circulation plasmon wave will constructively add to the other propagating waves. The same is true for the other structures displayed in Fig. 1, but as a result of the more complex shape, the plasmon propagation will be more complex and exhibit a smaller footprint. Additionally, new nearfield focuses will be introduced, for example at the structure centers. The structure geometries were analytically designed according to Lissajous type functions, or more specifically Epitrochoide geometries [12]. Using these functions, the geometries of the structures are defined according to the following equations:

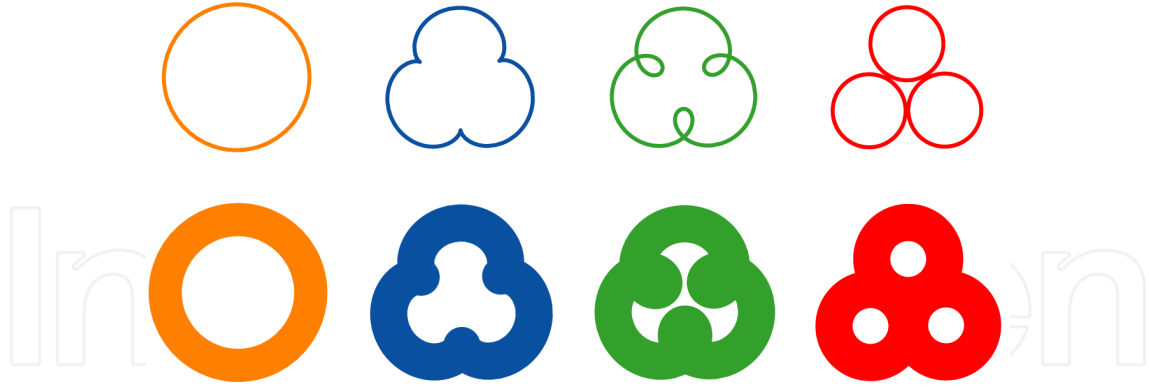


Figure 1. Sample designs of structures (top) and extended structure design for production (bottom) [12].

$$x = (R + r)\cos\phi - (r + \rho)\cos\left(\frac{R + r}{r}\phi\right) \quad (1)$$

$$y = (R + r)\sin\phi - (r + \rho)\sin\left(\frac{R + r}{r}\phi\right) \quad (2)$$

Where ϕ is an angle between 0 and 2π , r is the radius of a circle that is rotated about the boundary of a larger circle of radius R , and ρ is the distance from the outer boundary of the smaller circle to its center. Numerous variations of the above described structures were manufactured in arrays using EBL [13], and were prepared as follows:

Following a 200°C , 1 hour bake, ZEP 520 photo-resist was spun on to silicon plates to a thickness of 100 nm. The desired structures designs were then written onto the photo-resist using a Joel JBX-6000FS/E EBL system and subsequently etched (with SF_6 and C_4FH) to reveal the desired surface profile. Following this, a 5 nm thick adhesion layer of Platinum was deposited, and finally an 80 nm thick silver film deposition, to facilitate SPP excitation, was made. The overall array size was typically $200\ \mu\text{m}^2$ to $400\ \mu\text{m}^2$ (varying with sample scale and grating constant), meaning the overall arrays were typically visible by eye; their visibility aided by their natural diffraction. In the majority of the samples, these geometries represent the shape of the raised topography. However, in one manufacturing phase, the geometries represent lowered (trough) locations resulting in "rotor" shaped nanostructures; the importance of which will be discussed in section 4 of this chapter.

2.3. Farfield optical analysis

The characterisation of the structured arrays begins with a farfield diffraction analysis, using a semi-spherical scanner [Fig. 2]. Here, the sample was mounted on a sample goniometer, and was illuminated with a polarised laser (HeNe or Ti:Sa). Prior to incidence on the sample, the laser beam was also passed through an iris to reduce the beam diameter to approximately 0.5 mm (slightly larger than the typical size of the structure arrays). Additionally, for CW laser operation, a Fresnel Rhombus was placed in the laserline between the polariser and the iris, allowing for variation of the polarisation with no intensity dependence related to a fundamental polarisation preference of the laser. The detector used (photomultiplier tube) was positioned behind an aperture which had an azimuthal angular acceptance of 0.15° [Fig. 2].

Performing farfield diffraction characterisation allows for the quantification of the quality of the sample from both a plasmon perspective, and sample quality. An example of a complete θ, ϕ farfield scan is presented in Fig. 3a. The sample examined is an array of the 3-fold symmetric shamrock shaped design (grating constant of $1.5 \mu\text{m}$). Here, the sample was examined under P polarisation illumination, and with the sample goniometer at angles of $\theta = 45^\circ$, $\phi = 0^\circ$ and $\alpha = 45^\circ$ (diffraction pattern rotated by 45° to its normal). Series of scans such as this allow for the identification of SPP resonances (see section 4), checking the array pitch by measuring the diffraction angles, and making some sample quality checks, related to the sharpness of the diffraction and reflection channels. Using the scanner, high resolution mapping of individual diffraction orders is possible, enabling detailed characterisation of the spatial intensity distributions of the diffraction orders. Similar analysis (called spot analysis) is widely used in low energy electron diffraction (LEED) and related surface science techniques, where it permits the characterisation of the reciprocal space structure of a surface at atomic resolutions. However, the use of spot analysis is rarely used in visible laser spectroscopy techniques, as employed here. One such spatial intensity scan is presented in Fig. 3b, for a shamrock sample under P polarisation illumination, and with the sample goniometer at angles of $\theta = 55^\circ$, $\phi = 0^\circ$ and $\alpha = 0^\circ$. Immediately visible from the farfield intensity map is that the spot does not have a uniform (Gaussian) spatial distribution. This spatial distribution is not generated by the laser beam profile, which is close to (as a result of the small aperture) a Gaussian profile which is spatially cut approximately half way down its wings. This was confirmed by examining the laser profile of the reflection and diffraction from a symmetric ring shaped structure. This comparative check of the farfield spatial intensity profile of the ring structure and the shamrock structure confirms that the uneven spatial profile in Fig. 3b is as a result of the nanostructures symmetry properties. This is further confirmed by performing a Fast Fourier Transform (FFT) on the image, which reveals 6 preferential symmetry directions, directly related to the 3 fold symmetry of the nanostructures [Fig. 3c].

3. PEEM as a tool for imaging plasmonic fields

In this section, a nearfield examination of the plasmon enhanced electromagnetic fields on the above discussed reduced symmetry structures will be presented. For this, a PEEM (photo emission electron microscope) is used to map the plasmon nearfields on the surface

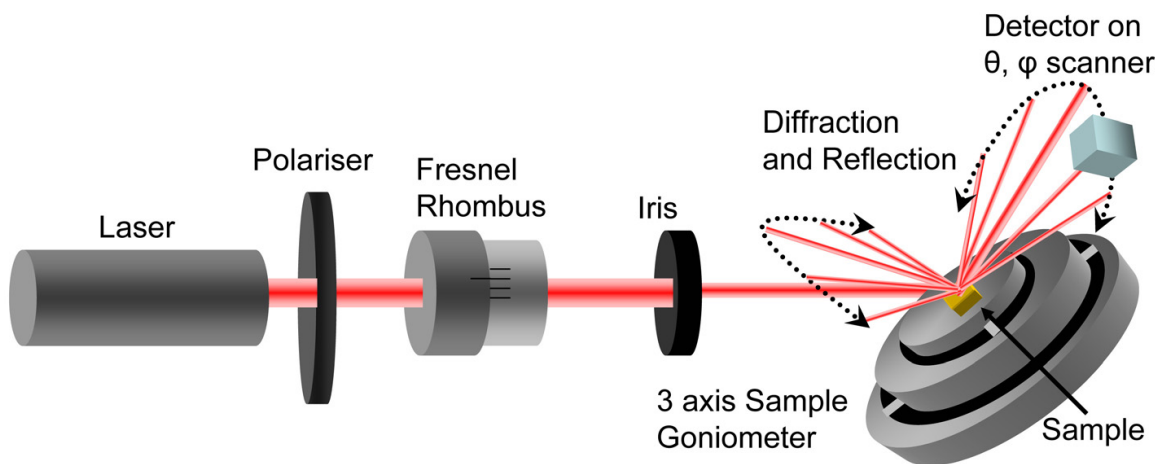


Figure 2. Set-up for farfield diffraction pattern (and individual diffraction spot) analysis [14].

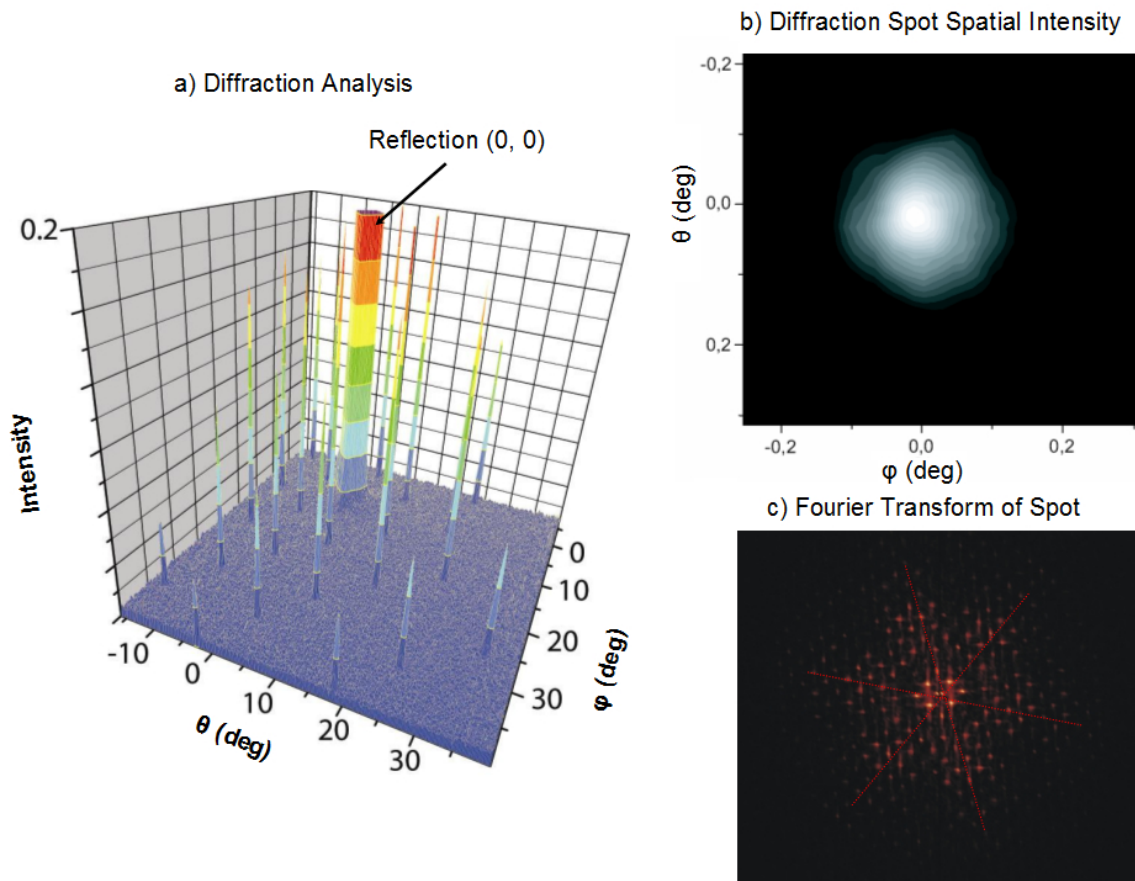


Figure 3. FIX C a) Sample diffraction characterisation. Reflection taken as the $(\theta, \phi) = (0, 0)$ point, θ and ϕ are the scan angles. b) High resolution farfield angular intensity map of single diffraction order (0, -2) from a 3-fold symmetric shamrock structure. c) Fast Fourier Transformation (FFT) of (b) demonstrates 3 preferential symmetry directions (indicated by dotted red lines) of the intensity spot, as a result of three fold symmetry of the structure [14].

of an array of threefold symmetric structures. In addition to the experimental observation of plasmon energy localization control [2], the powerful use of a PEEM for the non-perturbative subdiffraction limited imaging of plasmonic fields will be discussed.

3.1. Nearfield imaging

At the heart of much plasmon research are tools that allow researchers to examine plasmon effects in the nearfield. This was initially made possible with the development of scanning probe techniques, and their modification for the purpose of examining nearfield SPP properties directly at the surface at which the SPP is confined. The first scanning probe technique applied to the investigation of SPPs was scanning tunneling microscopy (STM), relying on the detection of changes to the tunnel current by SP induced variations in the local density of states [15–18] or the farfield scattered light due to the local SPP interaction with a STM tip [19].

Now, a wide range of techniques for the imaging of sub diffraction scale plasmon processes are available, with Scanning Nearfield Optical Microscopy (SNOM, or sometimes NSOM) being the most popular. This is a technique for optical investigation below the farfield resolution

limit (diffraction limit), which is achieved by exploiting the properties of evanescent waves. The technique involves placing the detector (typically a very small probe) very close (distance smaller than the wavelength) to the specimen surface, allowing for surface inspection with high spatial resolving power. With this technique, the resolution of the image is not limited by the wavelength of the illuminating light, but rather by the size of the detector probe, along with other considerations.

Irish scientist E. H. Synge is given credit for conceiving and developing the idea for an imaging instrument that would image by exciting and collecting diffraction in the nearfield. His original idea, proposed in 1928 [20, 21], was based on the usage of intense planar light from an arc under pressure behind a thin, opaque metal film with a small aperture of about 100 nm. The aperture was to remain within 100 nm of the surface, and information was to be collected by point by point scanning. He foresaw the illumination and the detector movement being the biggest technical difficulties [22].

Current generation SNOM techniques are very powerful tools for studying SPPs; however the perturbation and alteration of the SPP field associated with the introduction of a tip is one of the major concerns and drawbacks of SNOM techniques. The use of probes (coated or uncoated fibers, or SPM tips etc) in the nearfield proximity of metal surface results in a perturbation of the electromagnetic field due to the tip / surface interaction. However, until recently, there was no known way to investigate the nearfield plasmon information without influencing the plasmon itself to some extent with the measurement device.

However, in 2005, two independent groups demonstrated the use of a PEEM for the observation of plasmonic nearfields [23, 24]. In PEEM [Fig. 4c], photo-electrons emitted from the surface of a metal are imaged with electron optics, and these electrons are collected at a distance on the millimeter scale, meaning there is no influence of the collection optics on the plasmon before or during measurements.

PEEM is closely related to the more recently developed Low Energy Electron Microscopy (LEEM), with the predominant difference being that the principle of PEEM is the photoelectric effect. PEEM has already proven to be a powerful tool in material science, surface physics and chemistry, thin film magnetism, polymer science, and biology [25]. Historically, the invention of PEEM dates to the early 1930's, shortly after the introduction of electron lenses. The first working PEEM was built by Bruche in 1932, and the principal design of his PEEM is still used. In Bruche's PEEM, UV light from a mercury lamp was focused onto a sample, and the emitted photoelectrons were accelerated by a potential difference of 10 to 30 kV between the sample (cathode) and the anode of the PEEM, and subsequently focused onto a phosphor screen. A PEEM forms an image of a surface based on the spatial distribution of photoelectrons emitted. Importantly for plasmonics, photoelectron emission has been shown to be enhanced by the increase of the local electrical field upon excitation of SPPs [26].

The PEEM system we have in our lab is a SPECS PEEM P90, and depending on the photo-emission flux, this system is capable of imaging with a lateral resolution of 5 nm. The illumination frequency at which one can operate is dependent on the sample work function, which the illumination energy must be above for direct photoelectron mapping. Therefore, PEEM imaging of direct (or single) photo-emission processes presents a high resolution map of the surface workfunction threshold. For most plasmonic experiments, the surface under investigation is largely a smooth single material surface, with specifically designed sharp nanoscale structures for controlling the plasmons. On such a surface, the dominant variations

in workfunction arise from the sharp topographic variations, and so these can be mapped with high resolution using single photoelectron PEEM imaging. In order to map the plasmon nearfields, multiphoton photoelectron emission is used (typically 2 Photon Photo-Emission - 2PPE). This imaging technique is particularly useful for the imaging of plasmon effects, as the local multiphoton photo-emission is extremely sensitive to local field intensities (it varies with the square of the field strength), which are dramatically stronger at plasmon localised points [23, 24, 27].

A comparison of imaging plasmons using the PEEM technique to SNOM techniques reveals a number of advantages and disadvantages:

Advantages:

First and foremost, PEEM has the ability to image the plasmon without perturbing the plasmon field. By comparison, SNOM techniques require placing a probe within the plasmon field, and so inherently altering the field.

Unlike SNOM, PEEM is not a scanning imaging technique. Like an optical microscope, it captures all field information simultaneously, but with nanometer resolution. This means that the technique is extremely quick, allowing for real time, very fast monitoring of plasmons. In fact, the imaging rate is solely dependent on the required camera integration time, which is in turn dependent on the photoelectron emission rate, and ultimately on the illumination power.

As the 2PPE process is dependent on the square of the power of the local field strength, the contrast of the PEEM image is also a squared contrast. Therefore, to a first approximation, in a 2PPE PEEM image, an area that is twice as bright as another area, actually indicates that there is only a field strength difference of the square-root of the difference between the intensities. This squared dependence on the 2PPE results in a high contrast level when compared to SNOM techniques.

Disadvantages:

The main problem with PEEM is that the work function of typical plasmon active materials restricts 2PPE to the blue end of the visible spectrum, meaning that blue excited plasmons are most appropriate. However, with higher power systems (e.g. amplified Ti:Sa systems) observation of plasmons excited at 800 nm would be possible with 3 photon photo-emission. In comparison, SNOM keeps a fundamental advantage here, where its performance increases as the excitation frequency is reduced, and significantly, it works very well at telecom frequencies.

Another disadvantage of PEEM is the associated cost of the equipment. Imaging photo-electrons requires extremely good vacuum conditions, which has a high associated cost, and also a relatively large space requirement. Additionally, the imaging optics, similar to those in a Transmission Electron Microscope (TEM) or Scanning Electron Microscope (SEM), are costly. Furthermore, for successful plasmon imaging with a PEEM, femtosecond laser systems are required for excitation; again a significant cost. A typical SNOM would cost considerably less, requiring a relatively low quality SPM as its basis (atomic scale resolution is not necessary or usable), simple CW laser light sources as illumination, and no vacuum requirements.

Despite these disadvantages of a PEEM system, the advantage and power of direct real time imaging without perturbing the plasmon field cannot be ignored.

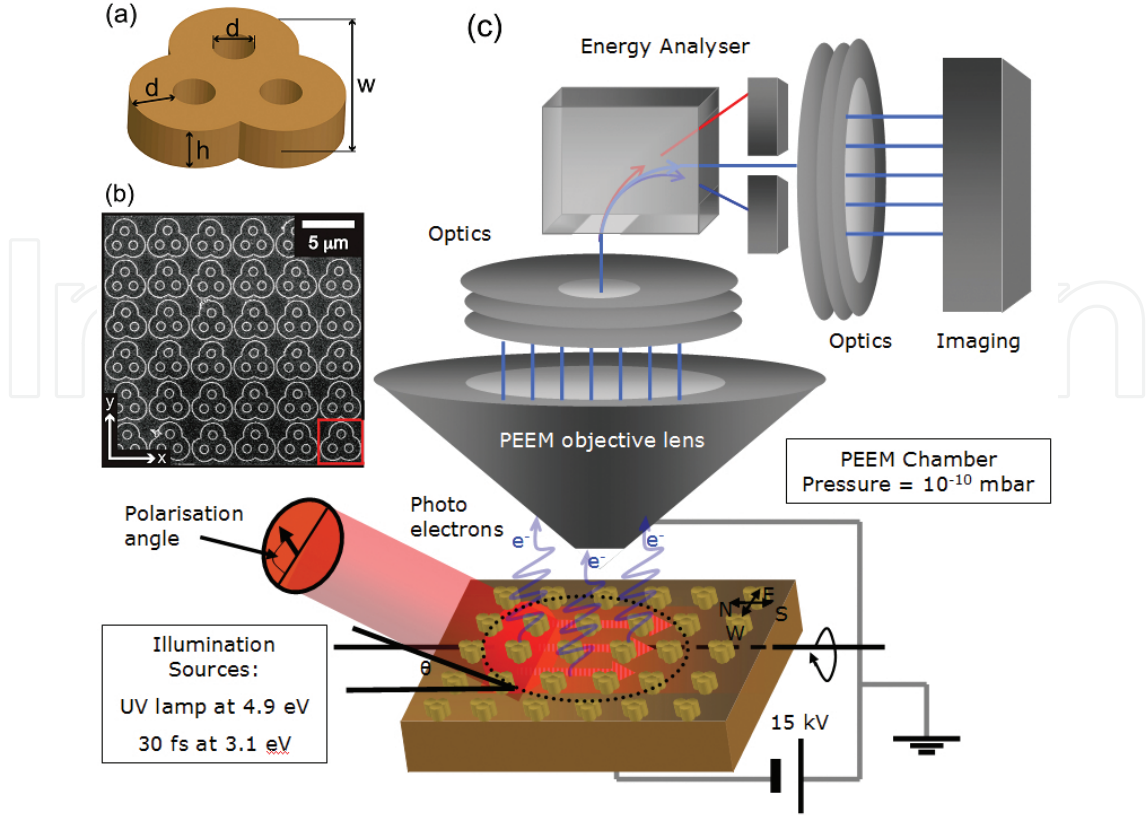


Figure 4. (a) Geometry of the structures. Structures in scale *A* have dimensions: $w = 2700$ nm, $d = 600$ nm, $h = 100$ nm; structures in scale *B* have dimensions $w = 3600$ nm, $d = 800$ nm, $h = 100$ nm. (b) SEM image of array of structures in scale *A* [2]. (c) Schematic of the technique for laser excited optical nearfield imaging with a PEEM [14]. For the presented results, the illumination angle (θ) is fixed at 25° . Note: Not all PEEMs are equipped with an energy analyser as depicted here for a Specs 90 PEEM.

3.2. Nearfield analysis of 3-fold symmetric structures

SPPs are intrinsically accompanied by strong electromagnetic nearfields, and surfaces can be actively modified to influence the excitation conditions of SPPs and hence nearfields. In particular, the selective addressability of nearfields on a surface is of interest, as shown in a demonstration of adaptive nearfield shaping [27]. In the following section, an investigation of the SPP electromagnetic nearfields excited on some of the structures described above is presented; the geometry and dimensions of which are depicted in Fig. 4. To investigate the nearfield distributions of an array of these structures, a Focus IS PEEM was used, described in detail in [28]. To record the PEEM images, two different light sources were used: a mercury-discharge lamp (UV illumination) with high-energy cutoff at 4.9 eV and a frequency-doubled Ti:Sa laser system, delivering 400 nm (3.1 eV) pulses of 100 fs duration and 20 mW at 80 MHz repetition rate. While the energy of the UV illumination is sufficient for the electrons to overcome the work function of the structured silver surface of 4.64 to 4.74 eV [29], the energy of the laser photons is too low. Hence at least two photon processes are required to generate photoelectrons; i.e. two photon photo-emission (2PPE). The laser power bandwidth product coupled to the plasmon nearfield enhancement resulted in readily observable 2PPE processes. As discussed above, as these 2PPE processes are very sensitive to the intensity of nearfields, nonlinear PEEM becomes a highly suitable tool to investigate and map plasmonic nearfield processes.

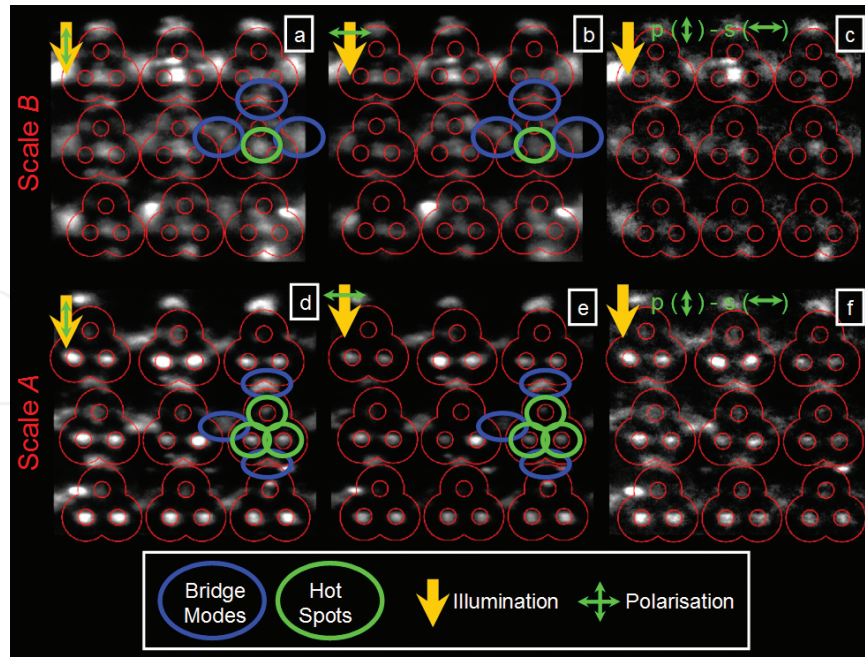


Figure 5. Contrast enhanced 2PPE PEEM images of a 3 by 3 cut out of the array of structures (a, b, d, and e). Images (c) and (f) show the differential image of S polarisation subtracted from P polarisation. 400 nm, ~ 100 fs laser illumination incident as indicated by yellow arrows (at an angle of $\theta = 25^\circ$). Polarisation is indicated by green arrows, P and S corresponding to vertical and horizontal respectively. For better recognition, the contour of the structures is highlighted (red). Deviations from the regular array pattern are due to spherical aberrations of the PEEM electron optics. Green circles represent hot spots as discussed in text and blue circles indicate bridge modes [2].

3.3. Plasmon energy localisation control observed by PEEM

For our presented investigation, firstly, the structures have been imaged using CW excitation at 4.9 eV to map the work function of the structure surface. These maps can be used as a reference for the 2PPE PEEM images to distinguish photo-emission effects due to the local electronic and morphologic structure of the sample surface from optical nearfields. Additionally, these work function images are used as a basis for aligning the actual structure geometries to the 2PPE PEEM images, whose size is independently confirmed by SEM (e.g. Fig. 4b) and AFM. Following this sample workfunction mapping, the structures have been investigated using the pulsed laser excitation for different illumination polarisation conditions. These 2PPE PEEM images were background subtracted and normalised via a sample independent reference beam on the microchannel plate in the imaging system of the PEEM, and subsequently contrast enhanced. In these images it is important to remember that intensity differences do not correlate linearly to the nearfield intensities, as discussed above. From these 2PPE PEEM images [Fig. 5], we can clearly identify nearfield plasmon effects. These excitations can be assigned to two different locations, at which they occur periodically across the entire array of structures:

Firstly, areas between the individual structures are excited, indicated by the bright intensities, which connect the structures of the array with each other vertically and horizontally. This emission occurs identically for structures of scales A and B, as highlighted by blue indicators in Fig. 5. These gap modes are due to field enhancement effects, which occur between the exposed edges of one structure towards its neighbors in the array.

Secondly, the other location where noteworthy enhancement takes place lies within the contour of the individual structures. These hot spots appear in each structure of the array. For scale A structures, these excitations are up to 280% brighter than the bridge excitations between the structures, depending predominantly on the intensity of the individual spot itself. This indicates an increased localisation of nearfield intensity in hot spots on the surface. Comparing Figs. 5a and 5d shows, additionally, that the strength and location of these excitations is dependent on structure size: for the larger structures the hot spots are located within the holes of the structure of the circles pointing along the x axis (there are no comparable excitations in the holes of the circles oriented in the y direction). Whereas, for the smaller structures the excitations are centered between the holes of the two circles along the x axis. Their intensity is much less pronounced and similar to the bridge excitations on the same array. Their excitation is promoted by geometric conditions resulting in the excitation of localized SPPs. The change of the location and intensity of the excitations within the contours of the individual structures is dependent on structure size and can hence be attributed to different interference and resonance conditions for the SPPs, determined purely by the geometric considerations.

To examine any polarisation dependence of these effects, P and S incident polarisations were examined for structures of both sizes. Images in Figs. 5a and 5d are acquired with P polarised light, images in Figs. 5b and 5e with S polarised illumination light. For comparison, S polarisation images are subtracted from P polarisation images [Figs. 5c and 5f]. The subtraction images demonstrate directly that the excitations within the contours of the individual structures generated with P polarisation have a stronger intensity than the ones generated with S polarisation for structures of both structure sizes. Surprisingly, the locations of the excitations are independent of the polarisation used. A quantitative analysis of the hot spots in the larger structures shows that the P intensity is about 50% higher than the S intensity. For the smaller structures the enhancement factor for the excitations within the contours of the structures varies in the range from 20% to 80%. The deviations in nearfield intensities from one structure to another can be attributed to the roughness peaks [30], but the location of the hot spots is predominantly determined by the geometric arrangement and shape of the structures.

3.4. Conclusion

A focusing of the SPP nearfields by threefold symmetrical to well defined locations is demonstrated. Observation of this effect is achieved using PEEM as a tool to map electromagnetic nearfields. The location of the focused nearfields varies with, and can be chosen by, the original structure size and design. More importantly, the intensity of locally fixed nearfields (hot spots) can be influenced by changing the polarisation of the excitation light by rotating the polarisation from S to P orientation. This enables one to switch the energy localisation on and off. Hence this approach presents a step towards a predictable design of structured surfaces, which focus energy in a spatially selective and switchable manner [2].

4. SPPs on 3-fold symmetry nanostructures

Of primary interest in this section are two arrays featuring nanostructures based on two different symmetry classes. The first array (the ring array) is designed with nanostructured rings invariant under C_∞ transformations and will be presented here as a reference array. In the second array (the rotor array), the structures resemble the shape of a triquetra rotor [Figs.

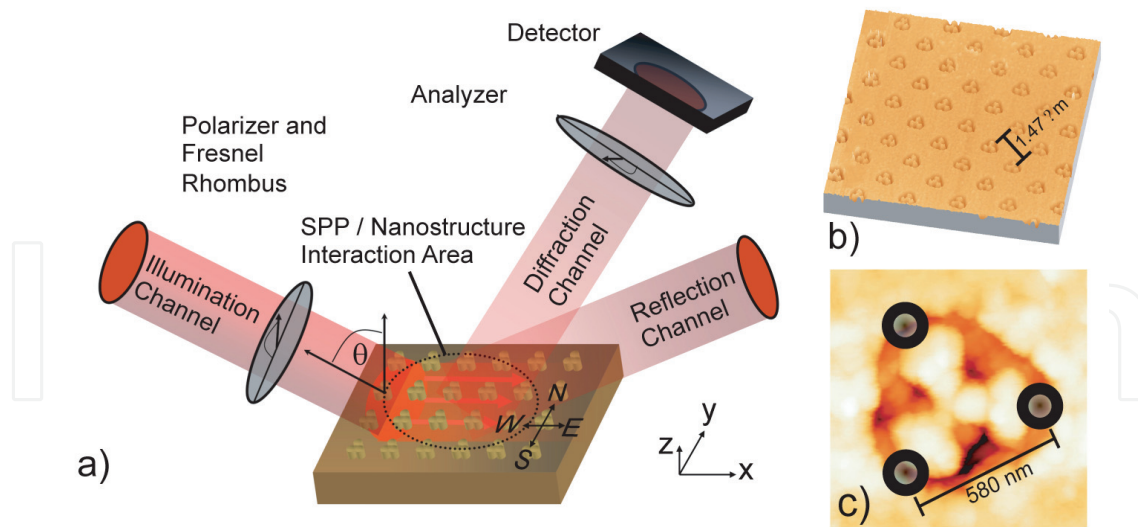


Figure 6. a) Visualisation of SPP excitation, propagation and re-emission processes, on a nanostructure arrayed surface [4]. Compass notation indicates the 4 examined interaction orientations - the displayed orientation in the schematic is E. b) AFM image of nanostructures array. c) Individual rotor structure including indication of scattering points used in the simulations.

6b and 6c]. They have a threefold symmetry and are invariant under C_3 transformations. The nanostructures are arranged to form a squared array, as indicated in Figs. 6a and 6b. As the rotor array is examined in four 90° separated orientations (α), compass notation (N, S, E, and W) will be used as identification labels [Fig. 6a]. Both arrays are housed on a 1 mm^2 silver coated section of silicon wafer and were prepared using e-beam lithography followed by etching to reveal the desired surface profile, as described above.

The experimental setup [Figs. 2 and 6a] for the farfield polarisation examination is as follows: A laser source ($\lambda = 632.8 \text{ nm}$) is collimated, polarised (extinction ratio of 10,000:1), and made incident on the sample which is housed on a rotation table on a fine adjust goniometer [Fig. 2]. A Fresnel Rhombus is positioned in the beam-line between the polariser and the sample. This allows for polarisation angle (β) variation with uniform beam intensity, independent of any fundamental polarisation of the laser. The detector (photodiode) is mounted on a computer controlled, highly resolving, angular scanner which has the sample goniometer at its fulcrum. A polarising analyser (extinction ratio of 10 000:1, analyser angle = γ) can be positioned on the semi-spherical scanner in front of the detector, depending on the experimental requirements.

4.1. Plasmon excitation on nanostructured arrays

Certain anomalies in the intensity of light diffracted from a grating are known to correspond to the excitation of SPPs [30]. They are apparent from sharp changes in the reflected intensity of P polarised light when the grating vector is parallel to the plane of incidence. In this case, the grating changes the in-plane wave vector of the incident photon field by the addition or subtraction of integer multiples of the grating wave vector [31, 32].

In order to locate the grating induced SPPs, angular scans for S and P polarisation were recorded in a direction about an axis parallel to the S oscillation, while maintaining the sample perpendicular to the laser in the plane of P oscillation. Such angular scans were carried out on a number of available diffraction orders for both samples in all four structure orientations. Here, for consistency and clarity, we predominantly limit our presentation to the

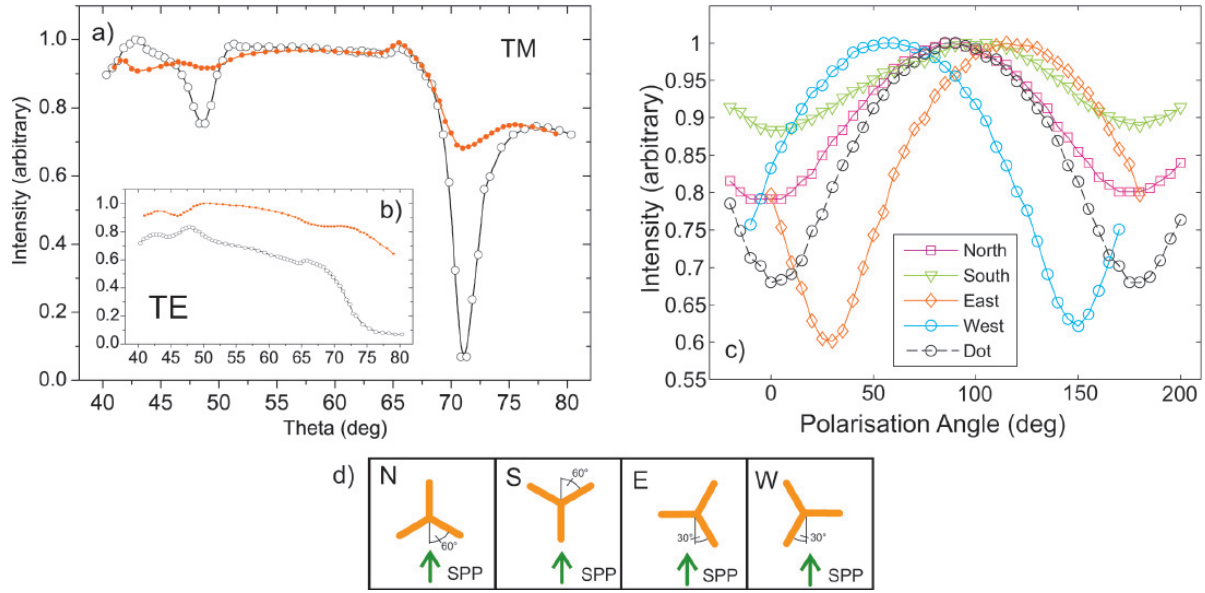


Figure 7. Angular scans of the intensity of the (+2, 0) diffraction order for the reference ring array (unfilled) and the rotor array in the North orientation (red, filled) for P (TM) polarised (a) and S (TE) polarised (b) light. c) Fixed angle polarisation scan for the ring array and for N,S,E and W orientations of the rotor array ($P = 0^\circ, 180^\circ$, $S = 90^\circ$). Note: The analyser indicated in Fig. 6a is absent for the results displayed in here. d) Four orientations of the rotors primary axis with respect to the excited propagating SPP [3].

(2, 0) diffraction order (however, the effect is not limited to this particular diffraction order [14]). For the reference (ring) array, the P polarisation curve reveals two pronounced minima at 71.3° and 48.5° , where the SPP extracts energy [Fig. 7a]. From this figure, it is clear that for the ring array the coupling efficiency for P polarised light is very strong; for the SPP at 71° , $I_{SPP}/I_{max} > 10\%$. For the rotor array, the excitation efficiencies at P polarised illumination are considerably lower than for the ring array. In terms of the angular resonance scan, the only effect the nanostructure design can have is on the efficiency at which light can be coupled to the surface. Generally, for a grating with single periodicity, the further one deviates from a sinusoidal cross-section profile, the lower coupling efficiency one gets, as a Fourier analysis of the profile reveals smaller (but broader) peaks [33].

4.2. SPP illumination polarisation dependence

As the ring array is completely invariant under 0° , 90° , 180° , and 270° rotations (α), angular scans at these orientations result in an identical plot to the corresponding plot in Fig. 7a. However, as a result of the 120° symmetry of the rotor structures, no overall 90° or 180° rotational symmetry is conserved. Therefore, if the structures themselves are to have an effect on the SPP resonance conditions, examinations with the structures in N, S, E, and W orientations should present individual differences. To this extent, it is observed that the rotor structures have a definite impact on the polarisation angle at which SPP related minimum reflectivities occur [Fig. 7c]. In order to investigate this phenomenon, the arrays were mounted at an angle such that the examined diffraction order was in resonance for P polarised light. The polarisation direction was subsequently rotated using the Fresnel rhombus in 5° increments through a full polarisation rotation. In contrast to such a scan using the ring array, which shows minimum reflectivity for purely P polarised light, for the rotor array it

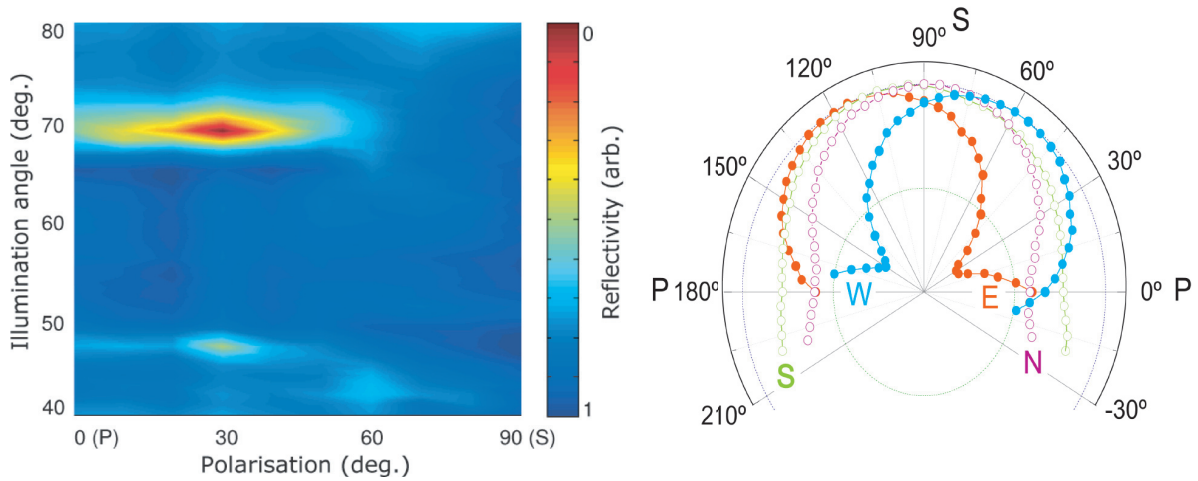


Figure 8. Left: Measured reflectivity for an illumination angular range, $\theta = 40^\circ$ to 80° , and illumination polarisation of P to S. Peaks at $\theta = 70^\circ$ and 47° indicate plasmon modes. Right: Intensity of the (+2nd) diffraction order as a function of polarisation angle (β) for rotor nanostructures in the 4 orientations (N, S, E, W) at the SPP excitation illumination angle ($\theta = 70^\circ$) [4]. Intensities are individually normalised to 1. Note: The analyser indicated in Fig. 6a is absent for the results displayed in these plots.

is observed that the minimum reflectivity does not necessarily occur for incoming P polarised light [Fig. 7c]. While the minimum reflectivities for N and S orientations are found at P polarisation, this is not the case for E and W orientations, where the minimum is shifted from P polarisation by $+30^\circ$ and -30° , respectively [3].

Before this illumination polarisation shift of the reflectivity minima can be confirmed to be solely a result of an interaction between propagating SPPs with the rotor structures, it must be confirmed that it is not purely a grating artifact; as it is well known that a complex grating topography can present changes in farfield intensity, independent of plasmonic effects [33, 35]. Therefore, we carried out a complete angular and illumination polarisation characterisation of our gratings for all 4 illumination orientations. An example of such an angular/polarisation scan for the SPP/rotor interaction in the E orientation is presented in Fig. 8; demonstrating that:

- The SPP excitations at illumination angles (θ) of 70° and 47° are the only pronounced intensity variations.
- For this SPP/nanostructure orientation (E) both plasmon reflectivity minima are shifted to a polarisation angle (β) of $\text{TM} + 30^\circ$.

From a qualitative point of view, an explanation of this shift of illumination polarisation corresponding to SPP related minimum reflectivity can be found in considering the symmetry of the structures with respect to the incoming illumination, and hence initial SPP propagation direction [Fig. 7d]. Turning our attention to processes occurring after excitation; consider the rotors in the E orientation. A grating induced SPP would propagate along the silver surface, where upon reaching the boundary of a rotor structure, the SPP wave would undergo a number of different processes with different probabilities [36]. As the SPP wave impinges on the boundary, the portion of the wave that is not transmitted or reradiated interacts with the boundary in two manners:

The first is through reflection [37, 38] and the second, and more interesting here, is through a guiding effect which can occur when a propagating SPP is made incident on a guiding surface feature [39–42]. It is anticipated that our triangular trough boundary acts much like

a waveguide; behaving as a gutter collecting the SPPs, and guiding them into propagation within the trough. This behaviour can only occur with relatively high efficiencies if there is an acute angle between the original SPP direction and the new guided direction, e.g. in analogy to skimming a stone on water. Following this, the SPP can be reradiated where its polarisation would be determined by the polarisation of the originally guided wave [43, 44]. As a result of the phase shift between the two optical channels contribution to this diffracted mode [45], these two light components will predominantly destructively interfere. Naturally, this destructive interference will be at a maximum where the polarisation states of the two interfering components are matching. It is important to remember that changing the incoming illumination polarisation angle does not change the associated polarisation orientation of the excited SPP; it only alters its relative excitation strength. For the rotor structure in the E orientation, for this polarisation matching to occur, the polarisation of the incoming light would be set to $P + 30^\circ$; matching the twist in the SPPs associated polarisation as described above. By a similar argument, with the rotors in the W orientation, this polarisation matching would occur at $P - 30^\circ$.

4.3. Plasmon mediated polarisation twisting

In order to investigate the origin and processes involved in this polarisation minimum shift, we have used a polariser/analyser set-up as in Fig. 6a. With the illumination angle set at the SPP excitation angle ($\theta = 70^\circ$), and the illumination polarisation set to P, we have recorded the intensity monitored by the detector, as a function of analyser polarisation. Such an examination would typically present a \cos^2 function of the angle between the polariser and the analyser. With the exception of an intensity offset, this is exactly what is observed for illumination angles off SPP resonance, and also for the symmetric SPP/nanostructure interaction orientations (N and S). However, for such a scan in the E and W orientations at the SPP excitation angle, we observe a deviation from a \cos^2 function [Fig. 9 left panel]. Most notably, we observe a 5° shift in analyser angle at which we observe a maximum. This deviation from a \cos^2 function indicates that our plasmon-rotor interaction is causing an additional polarising function. More specifically, this is proof that this interaction is twisting the polarisation of the light involved in the SPP excitation and re-emission process.

Although in this setup we observe a shift of only 5° , instead of the 30° shift observed in Fig. 8, both results are in fact consistent with each other. The apparent difference originates from that fact that one measurement takes into account SPP and regular diffraction channel processes, while the other isolates the SPP excitation processes [4].

This plasmon mediated polarisation twisting process is further confirmed by actively altering the distribution of light following the two paths. The variation in this ratio can be accurately controlled by tuning the illumination angle (θ), as presented in the right panel of Fig. 9. This plot of observed maxima in the polariser analyser experiment as a function of illumination angle, not only confirms the process of polarisation twisting, but also demonstrates the external active control over it that can be readily achieved (steps of 0.25° twisting readily realisable). Furthermore, the range of polarisation twisting could be greatly increased by improving both structure design and surface quality, currently limiting the SPP excitation efficiency to below 20%. If this excitation efficiency is increased, for example to 50%, the farfield measurable polarisation reorientation effect would be increased to 15° , and modifying the design of the structures to re-orientate the plasmon more efficiently would also increase the effect.

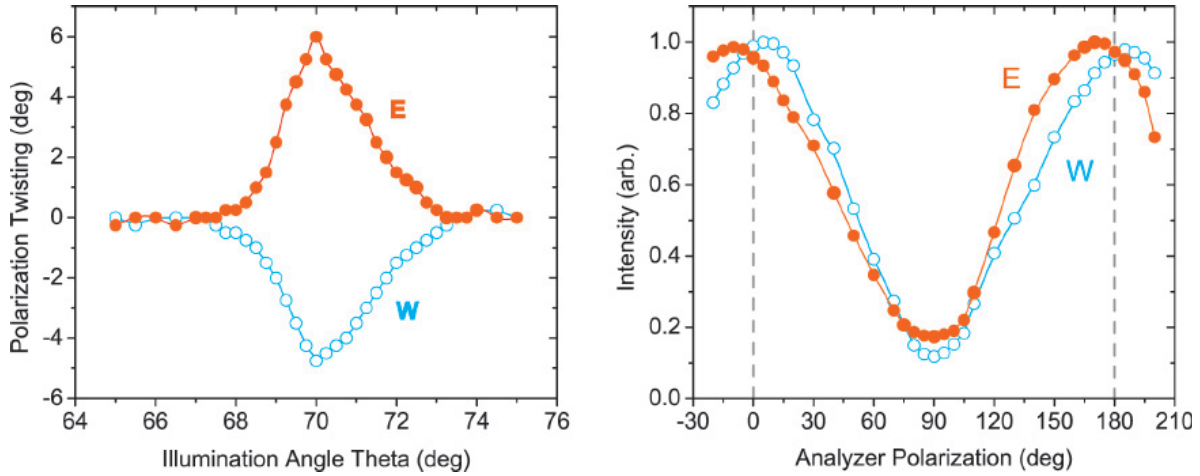


Figure 9. Left: Plot of normalised intensity as a function of analyser polarisation (γ), for illumination polarisation (β) of P. Right: Plot of polarisation twisting degree as a function of illumination angle (θ), for illumination polarisation of P [4].

4.4. Plasmon / rotor interaction simulations

To further understand the origin of the observed polarisation twisting, numerical simulations based on elastic SPP scattering [46] have been performed. In these simulations, we examine the interaction between the SPP associated electromagnetic field with the 120° symmetric structures. Initially, to allow us to focus solely on the origin of the polarisation twisting some simplifications of the processes contributing to the experimental observations have been deliberately made. This approach allows us to easily define and focus on the details we are interested in (namely the plasmon E field scattering) and so understand the real fundamental roots of polarisation twisting process. In these initial simulations performed by Dr. Vohnsen, a scalar effective polarisability representative of the scattering strength of each nanostructure has been used. Additionally, an ideal planar incident SPP has been assumed, absorption losses have been neglected (as these are negligible on the scale of an individual rotor structure), and for simplicity multiple SPP scattering between the structures has been omitted. By implementing these simplifications, a focus can be made on the origin of the plasmon E field re-orientation, which ultimately determines the polarisation re-orientation. Figs. 10a and 10d show results obtained with an individual rotor nanostructure in the N and W orientations and illuminated by an incident SPP from below. For the SPP incident in the W orientation, a change in the main E field direction of approximately 3° with respect to the direction of incidence is observed. This is also observed where a array of the structures is considered, as shown in Fig. 10e. This is caused by the interference of the incident SPP and the asymmetric configuration of the three-particle rotor model. In comparison to Figs. 10a and 10b where no resultant redirection of the E field occurs, the redirection of the plasmon visible in Figs. 10d and 10e implies that the propagation direction of the plasmon on the surface is redirected. However, the grating conditions place strict restrictions on the direction (or channels) at which light can leave the grating. Indeed, it is the additional conditions imposed by the grating that enables a polarisation twisting that, importantly, is not accompanied by a farfield relocation (spatial shift) of the light. This is typically not the case, where the polarisation *and* spatial conditions of the light are defined by the plasmon E field prior to reradiation. Therefore, for our structures, the polarisation of the reradiated light is defined by the plasmon E field immediately prior to the reradiating process, but the spatial direction of the light is defined by the grating conditions. For this reason, we can label the effect we observe as a true polarisation twisting.

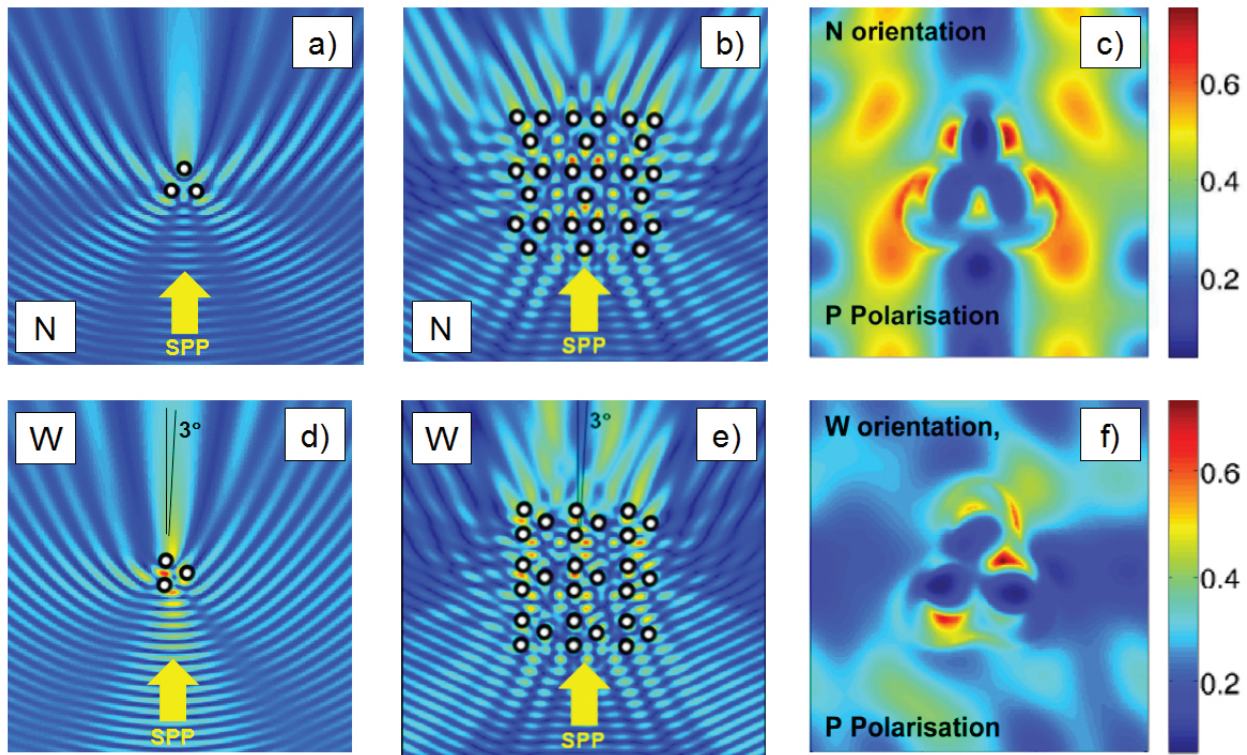


Figure 10. a&d) 10 x 10 micron field amplitude images of the incident and elastic scattered lossless SPPs, interacting with individual rotor representative structures in the N (a) and W (d) orientations [4]. b&e) Extension to interaction of SPPs with 3 by 3 arrays of the structures in the N (b) and W (e) orientations [14]. c&f) FDTD simulated nearfield energy distribution for the rotor structures in N (c) and W (f) orientations for P polarisation [5].

The difference in the degree of polarisation twisting between the experimental observations and the simulations is accounted for in the deliberate simplifications made in the simulations; especially in the substitution of the complex structures with just 3 scattering points. Regardless of these simplifications, the primary function of these simulations here is to identify and understand the dominating mechanisms contributing to the experimentally observed polarisation twisting. This has been confirmed to be as a result of an asymmetrical in-plane SPP scattering while the SPP/rotor interaction is in specific orientations (E and W). However, full FDTD calculations (by the group of Prof. Runge) demonstrate the experimentally observed 30° reorientation [5]. In these simulations, the near- and far-field properties of the rotor structure in the time-domain is calculated using the program FDTD solutions of Lumerical Solutions Inc. From these simulations, the electromagnetic nearfields, and the farfield reflectivities are calculated, as displayed in Figs. 10c and 10f. Importantly, as with the elastic SPP scattering simulations discussed above, in Fig. 10f a reorientation of the plasmon E field is again observed, but for these more complete simulations, the true degree of reorientation of ($\sim 30^\circ$) is apparent, corroborating the experimental findings presented above.

4.5. Conclusion

In this section, it has been shown that symmetry properties nanostructures can be designed to control the propagation of SPPs on the surface. In particular, it has been demonstrated and justified how in certain orientations, rotor shaped nanostructures have interesting wave-guiding interactions with propagating SPPs, resulting in a shift from P polarised

illumination at which the farfield SPP related minimum reflectivity occurs [3]. Building on this, the first instance of plasmon mediated polarisation reorientation observed in the farfield with no associated directional change of the farfield light was described. For this, an experimental demonstration of how tailor designed topographic structures of threefold symmetry can be used to alter the polarisation of an EM wave by a selective amount was made. It was isolated and confirmed that the primary process involved in this polarisation twist is from the interaction of a propagating SPP wave with the nanostructures. Specifically, the polarisation orientation of the light is determined by the **E** field orientation of the plasmon directly before its re-emission, and the farfield spatial location is determined by the grating conditions. This results in the observed polarisation twisting with no associated farfield directional change. The only apparent restrictions on the polarisation rotation are found to be the initial plasmon excitation conditions [4].

Finally, using Green's function based simulations, the interaction between a propagating plasmon wave and 120° three-fold symmetric structures was examined, confirming that the origin of the farfield polarisation twisting is an asymmetrical in-plane SPP scattering occurring in the nearfield. This computational observation is further confirmed by FDTD calculations of the same structures [5].

5. Ultrafast broadband plasmonics

Time scales associated with SPPs vary from 100's of attoseconds to 100's of nanoseconds. The lower limit is a theoretical limit defined by the inverse spectral width of a broadband plasmonic resonance [47], and is one of the fastest time scales in optics. However, as of yet, little experimental output has come from examining freely propagating plasmons at metal / dielectric interfaces on these ultrashort time scales. The reason for this is as a result of the combination of the difficulty in making accurate measurements on a suitable time scale, but more importantly, the difficulty in accessing plasmon modes of suitable bandwidth to support these ultrafast processes. Despite these difficulties, understanding these ultraquick processes is of key importance to the field of nanoplasmonics, and could have potential applications in, for example, ultrafast computations, and data control and storage on the nanoscale. Recently, a system that provides access to the efficient excitation of broadband, propagating plasmon modes, capable of supporting SPP pulses with temporal lengths on the 20 fs scale has been designed [6]. To achieve this feat, a surface array of tailor designed, reduced symmetry nanostructures has been specifically architected to enable the appropriate control of the plasmon dispersion relation.

5.1. Ultrafast plasmonics

The vast majority of the experimental work on ultrafast SPP dynamics have either dealt with temporal dephasing of particle plasmons [48–53], or have been aimed at understanding the processes through which unexpected levels of optical transmission in subwavelength perforated thin metal films occurs. Indeed, for the ultrafast dynamics of SPPs, the major focus of experimental research has been geared toward the understanding of extraordinary optical transmission (EOT); first observed in the visible regime by Ebbesen et al. [31]. The complete underlying processes of EOT is still somewhat of a debate [32, 54–57]; and as a result, in order to understand the process of EOT in more detail, researches have examined the temporal characteristics of EOT using ultrashort pulse illumination.

The first of these experimental examinations was carried out by the group of Ebbesen [58] where the transit time of a ~ 100 fs pulse passing through a metal film perforated with an array of subwavelength apertures was considered. Light transmitted through a subwavelength aperture was coherent with the incident pulse, and showed a 7 fs total transient time over the 0.3 mm layer of silver film. The authors report that these delay times support the general picture in which the resonant coupling of light with metallic surface modes is responsible for the relatively large transmission and the slow group velocity of light inside these subwavelength apertures. In the following years, further theoretical and experimental examinations were made based on similar designs, but instead of assigning this delay to the finite transit time for light propagation through the nanoholes, it was assigned to the SPP lifetime for such a structure. In a theoretical work studying the propagation of 10 fs pulses (shorter than the damping time of SP excitations at the interfaces of the metal film), pronounced temporal oscillations in the transmitted light were predicted [59]. It was concluded that these oscillations reflect the temporal character of the coupling of SPPs at both interfaces via photon tunneling through the nanohole channel. More recent experiments have also confirmed a modification of the dephasing rates due to interactions between localised particle plasmons and optical waveguide modes, and subsequent modification of the photonic density of states [60]. In [61] it was demonstrated that SP transmission peaks through the nanohole arrays were homogeneously broadened by the SP radiative lifetime. From the same group an experimental study of ultrafast light propagation through plasmonic nanocrystals using light pulses much shorter in duration than the SPP damping time, was made [62]. Here, phase-resolved measurements of the time structure of the transmitted light allowed for the identification of two different contributions to the EOT effect to be nonresonant tunneling and SPP re-radiation.

Other recent reports of specific significance on the topic of ultrafast SPP dynamics have used pump probe experiments, combined with SP induced photoelectron imaging (PEEM) to achieve nanoscale spatial, and femtosecond (even sub fs) temporal imaging. In [63], ultrafast laser spectroscopy and PEEM were combined to image the quantum interference of localised SP waves. This technique permitted imaging of the spatio-temporal evolution of SP fields with a 50 nm spatial resolution taken at a 330 as frame rate. Using a similar technique, SP dynamics in silver nanoparticles have been studied [26], and an investigation of the optical nearfield was demonstrated by mapping photoemitted electrons from specially tailored Ag nanoparticles deposited on a Si substrate [23]. While on the topic of active plasmon control, femtosecond optical switching of a propagating SPP signal was reported in [64]. Here, experimental examination and theoretical analysis show that femtosecond plasmon pulses can be generated, transmitted, modulated and decoupled for detection in a single device.

Regarding the future of ultrafast plasmonics; a number of publications have recently been made indicating some of the potential directions of nanoscale spatial and fs temporal plasmonics research [47, 65, 66]. One of the key requirements to achieve the potential that ultrafast plasmonics can offer is the ability to access plasmon modes of suitable bandwidth; this will be the focus of the next section.

5.2. Broadband ultrashort propagating plasmon pulses

For a typical Ti:Sa laser system, following group delay dispersion compensation, near transform limited (sub 20 fs) illumination pulses can be generated. In order to permit the excitation of SPP pulses of comparable temporal duration to such illumination pulses, the first requirement is that the SPP excitation mechanism simultaneously envelopes the

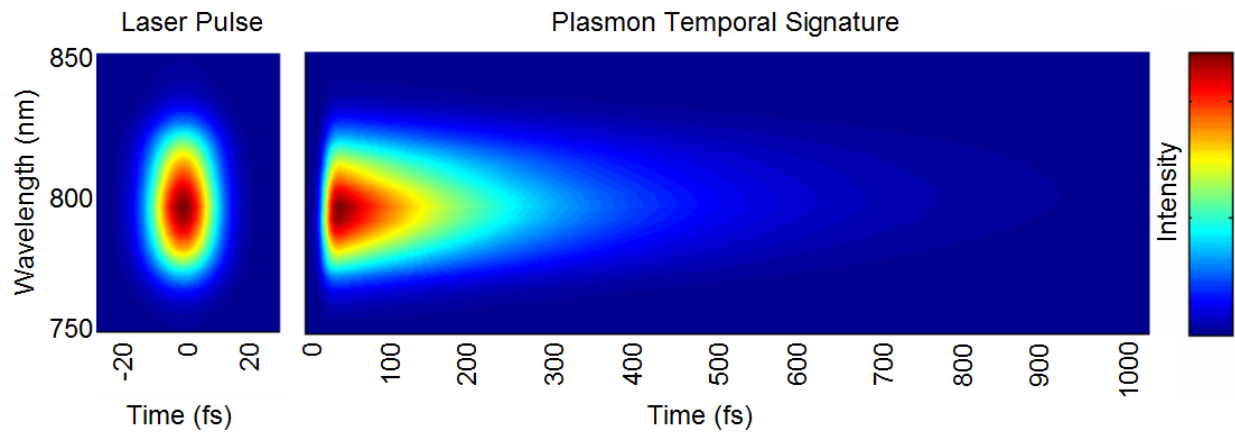


Figure 11. Simulation of the temporal signature of a broadband propagating SPP (right) driven by a sub 20 fs broadband laser pulse from a Ti:Sa laser (left).

complete spectrum of the illumination pulse. In order to spectrally envelope a sub 20 fs pulse bandwidth, an SPP coupling acceptance bandwidth exceeding 80 nm is required. Furthermore, for propagating plasmons, the illumination pulse must remain spatially and temporally optimized prior to interaction with the surface. This implies that the required broadband excitation mechanism must couple this complete illumination bandwidth at a single angle of incidence. However, for high efficiency SPP excitation architectures (i.e. typical grating or attenuated total reflection coupling) the SPP dispersion relation varies rapidly with illumination frequency and angle [30]. For example, in an ATR configuration, the full bandwidth of a spatially and temporally unchirped ultrashort pulse cannot be coupled to an SPP simultaneously [69], thus prohibiting the generation of SPP pulses of comparable duration to the driving ultrashort laser pulse. For some nanofeature based excitation mechanisms (e.g. nanoparticle, rough surface [30], slit [70], etc.) a suitable broad range of momenta can be inherently provided, allowing for broadband plasmon excitation. However, such excitation schemes are limited to comparably weak SPP generation [70], with only a very small percentage of the illumination light coupled to the desired SPP mode. Furthermore, such coupling techniques are not suitable for propagating plasmon pulse generation, as the excited plasmons will have a range of group and phase velocities, will not co-propagate, and so will be strongly spatially and temporally chirped. With these restrictions in mind, a primary research objective is to overcome these obstacles and realize a highly efficient broadband SPP excitation mechanism.

For the laser excitation wavelength of a Ti:Sa laser centered at 800 nm [67], the unperturbed SPP lifetime is ~ 230 fs for a silver / air interface. A theoretical prediction of the temporal evolution of a broadband SPP excited by a 20 fs broadband pulse is presented in Fig. 11. This simulation shows how a plasmon propagating on a silver surface would evolve and decay in time. It also demonstrates that on this planar silver / dielectric interface, the SPP dispersion relation implies that as the plasmon pulse propagates, its wavefront will become distorted due to the fact that the $1/e$ decay time ranges from approximately 155 fs at the blue end of the Ti:Sa spectrum (750 nm) to 260 fs at the red end (850 nm). This introduces an additional restriction on accessing non-distorting ultrashort plasmon pulses; as it means that a broadband plasmon propagating at a planar metal interface will always become chirped as it propagates.

Therefore, one of the primary challenges in ultrafast plasmonics is the design of a plasmon excitation mechanism that allows for the efficient excitation of broadband, non-distorting plasmon modes. As justified above, this feat will not be possible for planar interface

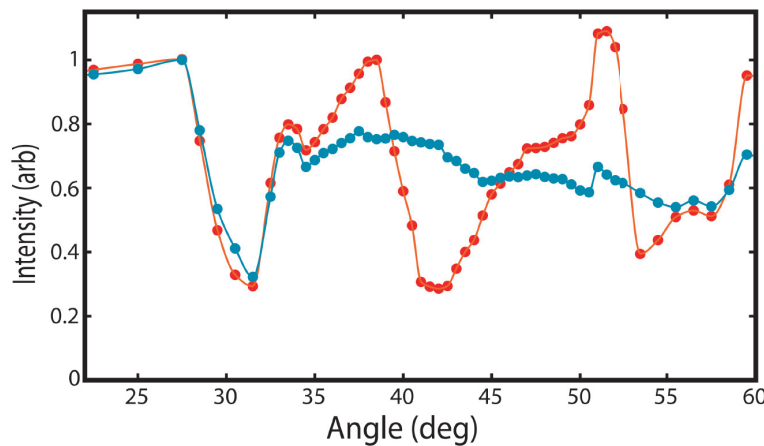


Figure 12. Intensity reflectivity scans for a 800 nm CW laser (red) and a broadband (centered at 800 nm) sub 20 fs laser (blue). Three pronounced plasmonic modes are apparent for CW light located at 31°, 42° and 55°, but only one pronounced mode is visible for the broadband pulse at 31°.

arrangements. Thus, in order to achieve this goal, our experiments deal with SPP excitation on an array of reduced symmetry nanostructures. The initial design for the structures was conceived and optimized using reciprocal space analysis. The geometry was chosen to present a range of inter-structure distances to suit the near Gaussian spectral distribution of the laser, and the physical dimensions of the surface features were optimized for SPP excitation in the near IR [6].

Confirmation of SPP excitation in these tailor designed nanostructured arrays for CW light (at 800 nm) and sub 20 fs pulses of broadband light (at 760-840 nm) is presented in Fig. 12. Three SPP modes are clearly identifiable (as reflectivity minima) for the CW laser excitation at 31°, 42° and 55°. However, for the broadband source, only one sharp SPP mode at 31° is apparent. Importantly, because the plasmon mode at 31° appears identical for both broadband and CW light sources, this indicates that this mode has at least a comparable bandwidth to the broadband source. For such grating excited plasmons, it is typically not possible to excite SPPs of comparable bandwidth to a sub 20 fs Ti:Sa laser. This is because of a strong momentum variation typically exhibited by plasmon modes over such a broad spectrum; as is the case for the modes at 42° and 55° observed only for the CW scan in Fig. 12. However, for SPP excitation on the array of reduced symmetry nanostructures it is found that a plasmon mode whose angular variation over the spectral range is very low is accessible [6]. Indeed, this mode has been found to be suitable for broadband plasmon excitation, coupling the complete illumination spectrum of a 17.5 fs, Ti:Sa system. Further angular and spectral examinations of the excitation of SPPs confirm the presence of multiple plasmonic modes for the CW source; but importantly they also reveal multiple modes for the broadband source. These additional modes are found to have the typical strong spectral variation [30], and so are not suitable for broadband SPP excitation. However, for the mode at 31° plasmons of very high bandwidth (and so very short temporal characteristics) can be excited [6].

5.3. Conclusion

In final section, a method for the excitation of broadband plasmonic modes in the near-IR regime was presented [6]. This has been achieved using a tailor designed reduced symmetry periodic surface that grants access to an SPP mode which has a fixed momentum value over

the entire bandwidth of an ultrafast Ti:Sa laser. For this sample, as a result of the well ordered array basis, a high SPP coupling efficiency is achieved, and as a result of the reduced symmetry nanostructures, the range of momenta provided by the grating in a fixed direction is increased, presenting the possibility of accessing efficient, co-propagating, broadband SPPs. This ability to generate broadband, ultrashort SPP pulses that exhibit no spatial or temporal chirping in their excitation is an important step toward accessing the previously predicted ultraquick optical processes associated with SPPs.

Acknowledgements

The majority of the work presented here is based on sections of the PhD thesis of Dr Brian Ashall, carried out under the supervision of Dr Dominic Zerulla.

The authors would like to thank Dr Michael Berndt, Prof. Martin Aeschlimann, Dr Brian Vohnsen, Prof. Erich Runge, Dr Jose Francisco Lopez-Barbera and Dr Stephen Crosbie for their valuable contributions. The authors acknowledge Science Foundation Ireland and Enterprise Ireland for ongoing funding of our research in the field of plasmonics.

Author details

Brian Ashall

School of Science, Technology, Engineering and Mathematics, Institute of Technology Tralee, Ireland

Dominic Zerulla

School of Physics, College of Science, University College Dublin, Belfield, Dublin 4, Ireland

6. References

- [1] H. A. Atwater, The Promise of Plasmonics, Scientific American, April Issue (2007).
- [2] M. Berndt, M. Rohmer, B. Ashall, C. Schneider, M. Aeschlimann, and D. Zerulla, Opt. Lett., 34:959 (2009).
- [3] B. Ashall, M. Berndt, and D. Zerulla, Appl. Phys. Lett., 91: 203109 (2007).
- [4] B. Ashall, B. Vohnsen, M. Berndt, and D. Zerulla, Phys. Rev. B, 80:245413 (2009).
- [5] D. Leipold, S. Schwieger, B. Ashall, D. Zerulla, and E. Runge, Photonics and Nanostructures 8 297 (2010).
- [6] B. Ashall, J. F. Lopez-Barbera, and D. Zerulla, Manuscript submitted to New Journal of Physics (2012).
- [7] J. Melngailis, J. Vac. Sci. Technol. B, 5, 469 (1987).
- [8] D. K. Stewart, A. F. Doyle, and J.D. Jr Casey, Proc. SPIE, 276, 4337 (1995).
- [9] B. W. Ward, N. P. Economou, D. C. Shaver, J. E. Ivory, M. L. Ward, and L. A. Stern, Proc. SPIE, 92, 923 (1988).
- [10] T. H. Taminiau, R. J. Moerland, F. B. Segerink, L. Kuipers, and N. F. van Hulst, Nano Lett., 7, 28 (2007).
- [11] X. Jiao, J. Goeckeritz, S. Blair, and M. Oldham, Plasmonics, 4, 37 (2009).
- [12] M. Berndt, Anregung von Oberflächenplasmonen auf mesoskopischen Strukturen, Diploma Thesis, Heinrich-Heine-Universität, Düsseldorf, (2007).
- [13] EBL system available via the National Access Program, Tyndall National Institute in Cork.
- [14] B. Ashall, Surface Plasmon Polaritons on Nanostructures Surfaces, Doctor of Philosophy Thesis, University College Dublin (2009).

- [15] R. Möller, U. Albrecht, J. Boneberg, B. Koslowski, P. Leiderer, and K. Dransfeld, *J. Vac. Sci. Technol. B*, 9, 506 (1991).
- [16] N. Kroo, J.P. Thost, M. Völcker, W. Krieger, and H. Walther, *Europhys. Lett.*, 15, 289 (1991).
- [17] D.W. Pohl and D. Courjon, *Near Field Optics*, Kluwer, (1993).
- [18] I. I. Smolyaninov, A. V. Zayats, and O. Keller, *Phys. Lett. A*, 200, 438 (1995).
- [19] M. Specht, J.D. Pedarnig, W.M. Heckl, and T.W. Hansch, *Phys. Rev. Lett.*, 68, 476 (1992).
- [20] E. H. Synge, *Phil. Mag.*, 6, 356 (1928).
- [21] E. H. Synge, *Phil. Mag.*, 13, 297 (1932).
- [22] B. Hecht, B. Sick, U. P. Wild, V. Deckert, R. Zenobi, O. J. F. Martin, and D. W. Dieter, *J. Chem. Phys.*, 18, 112 (2000).
- [23] M. Cinchetti, A. Gloskovskii, S. A. Nepjiko, G. Schönhense, H. Rochholz, and M. Kreiter, *Phys. Rev. Lett.*, 95, 047601 (2005).
- [24] A. Kubo, K. Onda, H. Petek, Z. Sun, Y. S. Jung, and H. K. Kim, *Nano Letters*, 5, 1123 (2005).
- [25] J. Feng and A. Scholl, *Science of Microscopy - Chapter 9: Photoemission Electron Microscopy*, Springer New York (2007).
- [26] J. Lehmann, M. Merschdorf, W. Pfeiffer, A. Thon, S. Voll, and G. Gerber, *Phys. Rev. Lett.*, 85, 2921 (2000).
- [27] M. Aeschlimann, M. Bauer, D. Bayer, T. Brixner, F. J. García de Abajo, W. Pfeiffer, M. Rohmer, C. Spindler, and F. Steeb, *Nature*, 446, 301 (2007).
- [28] M. Munzinger, C. Wiemann, M. Rohmer, L. Guo, M. Aeschlimann, and M. Bauer, *New J. Phys.*, 7, 68 (2005).
- [29] H. B. Michaelson, *J. Appl. Phys*, 48, 4729 (1977).
- [30] H. Raether, *Surface Plasmons on Smooth and Rough Surfaces and on Gratings*, Springer Verlag, Berlin (1988).
- [31] T. W. Ebbesen, H. J. Lezec, H. F. Ghaemi, T. Thio, and P. A. Wolff, *Nature*, 391, 667 (1998).
- [32] H. F. Ghami, T. Thio, D. E. Grupp, T. W. Ebbesen, and H. J. Lezec, *Phys. Rev. B*, 58, 6779 (1998).
- [33] R. Petit, *Electromagnetic Theory of Gratings*, Springer Berlin, Springer Topics in Current Physics Vol 22 (1980).
- [34] S. Rehwald, M. Berndt, F. Katzenberg, S. Schwieger, E. Runge, K. Schierbaum, and D. Zerulla, *Phys. Rev. B*, 76, 085420 (2007).
- [35] C.H. Wilcox, *Scattering Theory for Diffraction Gratings*, Springer Berlin, Springer Applied Mathematical Sciences Vol 46 (1984).
- [36] G. I. Stegeman, A. A. Maradudin, and T. S. Rahman, *Phys. Rev. B*, 23, 2576 (1981).
- [37] R. F. Wallis, A. A. Maradudin, and G. I. Stegeman, *Appl. Phys. Lett.*, 42, 764 (1983).
- [38] P. Dawson, F. de Fornel, and J-P. Goudonnet, *Phys. Rev. Lett.*, 72, 2927 (1994).
- [39] Y. Satuby and M. Orenstein, *Appl. Phys. Lett.*, 90, 251104 (2007).
- [40] S. I. Bozhevolnyi, J. Erland, K. Leosson, P. M. W. Skovgaard, and J. M. Hvam, *Phys. Rev. Lett.*, 86, 3008 (2001).
- [41] S. I. Bozhevolnyi, V. S. Volkov, K. Leosson, and A. Boltasseva, *Appl. Phys. Lett.*, 79, 1076 (2001).
- [42] B. Steinberger, A. Hohenau, H. Ditlbacher, A. L. Stepanov, A. Drezet, F. R. Aussenegg, A. Leitner, and J. R. Krenn, *Appl. Phys. Lett.*, 88, 094104 (2006).
- [43] G. Isfort, K. Schierbaum, and D. Zerulla, *Phys. Rev. B*, 73, 033408 (2006).
- [44] G. Isfort, K. Schierbaum, and D. Zerulla, *Phys. Rev. B*, 74, 033404 (2006).
- [45] J. M. Pitarke, V. M. Silkins, E. V. Chulkov, and P. M. Echenique, *Rep. Prog. Phys.*, 70 (2007).

- [46] S. I. Bozhevolnyi and V. Coello, *Phys. Rev. B*, 58, 10899 (1998).
- [47] M. I. Stockman, M. F. Kling, U. Kleineberg, and F. Krausz, *Nat. Photon.*, 1, 539 (2007).
- [48] C. Sönnichsen, T. Franzl, T. Wilk, G. von Plessen, J. Feldmann, O. Wilson, and P. Mulvaney, *Phys. Rev. Lett.*, 88, 077402 (2002).
- [49] B. Lamprecht, J. R. Krenn, A. Leitner, and F. R. Aussenegg, *Phys. Rev. Lett.*, 83, 4421 (1999).
- [50] B. Lamprecht, A. Leitner, and F. R. Aussenegg, *Appl. Phys. B*, 68, 419 (1999).
- [51] A. Wokaun, J. P. Gordon, and P. F. Liao, *Phys. Rev. Lett.*, 48, 957 (1982).
- [52] T. Klar, M. Perner, S. Grosse, G. von Plessen, W. Spirkel, and J. Feldman, *Phys. Rev. Lett.*, 80, 4249 (1998).
- [53] J. Bosbach, C. Hendrich, F. Stietz, T. Vartanyan, and F. Trager, *Phys. Rev. Lett.*, 89, 257404 (2002).
- [54] U. Schroter and D. Heitmann, *Phys. Rev. B*, 58, 15419 (1998).
- [55] J. A. Porto, F. J. Garcia-Vidal, and J. B. Pendry, *Phys. Rev. Lett.*, 83, 2845 (1999).
- [56] T. Thio, H. F. Ghaemi, H. J. Lezec, P. A. Wolff, and T. W. Ebbesen, *J. Opt. Soc. Am. B*, 16, 1743 (1999).
- [57] M. M. J. Treacy, *Appl. Phys. Lett.*, 75, 606 (1999).
- [58] A. Dogariu, T. Thio, L. J. Wang, T. W. Ebbesen, and H. J. Lezec, *Opt. Lett.*, 26, 450 (2001).
- [59] R. Müller, V. Malyarchuk, and C. Lienau, *Phys. Rev. B*, 68, 205415 (2003).
- [60] T. Zentgraf, A. Christ, J. Kuhl, and H. Giessen, *Phys. Rev. Lett.*, 93, 243901 (2004).
- [61] D. S. Kim, S. C. Hohng, V. Malyarchuk, Y. C. Yoon, Y. H. Ahn, K. J. Yee, J. W. Park, J. Kim, Q. H. Park, and C. Lienau, *Phys. Rev. Lett.*, 91, 143901 (2003).
- [62] C. Ropers, Müller, C. Lienau, G. Stibenz, G. Steinmeyer, D.-J. Park, Y.-C. Yoon, and D.-S. Kim, *Ultrafast dynamics of light transmission through plasmonic crystals*, International Conference on Ultrafast Phenomena, Niigata, Japan (2004).
- [63] A. Kubo, K. Onda, H. Petek, Z. Sun, Y. S. Jung, and H. K. Kim, *Nano Lett.*, 5, 1123 (2005).
- [64] K. F. MacDonald, Z. L. Sármson, M. I. Stockman, and N. I. Zheludev, *Nature Photonics*, 3, 55 (2008).
- [65] M. I. Stockman, *N. J. Phys.*, 10, 025031 (2008).
- [66] J. Lin, N. Weber, A. Wirth, S. H. Chew, M. Escher, M. Merkel, M. F. Kling, M. I. Stockman, F. Krausz, and U. Kleineberg, *J. Phys.: Condens. Matter*, 21, 314005 (2009).
- [67] Griffin C Ti:Sa Laser, Kapteyn-Murnane Laboratories Inc.
- [68] R. Trebino, *Frequency-Resolved Optical Gating: The Measurement of Ultrashort Pulses*, Kluwer Academic Publishers (2000).
- [69] S. E. Yalcin, Y. Wang, and M. Achermann, *Appl. Phys. Lett.*, 93, 101103 (2008).
- [70] J. Chen, Z. Li, M. Lei, S. Yue, J. Xiao, and Q. Gong, *Opt. Exp.*, 19, 26463 (2011).